Supplement of Atmos. Meas. Tech., 13, 2865–2886, 2020
https://doi.org/10.5194/amt-13-2865-2020-supplement

Atmospheric Measurement Techniques
Open Access
EGU

Supplement of

Development of a new correction algorithm applicable to any filter-based absorption photometer

Hanyang Li et al.

Correspondence to: Andrew A. May (may.561@osu.edu)

This Word document includes:

SUPPLEMENTARY TEXT

1. Developing the model described in Section 2.4.4

Statistical regression analyses were performed to predict $\frac{B_{abs}}{B_{ATN}}$ (dependent variable) in Eq. (9). The analyses were applied on a total of 2676 FIREX observations (PAX-derived B_{abs}, CLAP-derived B_{ATN}, Tr, SSA, and AAE) at three wavelengths (467 nm, 528 nm, and 652 nm). Table S1 summaries the variables used in the analyses. The statistical software R was used for all analyses.

Table S1 Descriptive statistics for the variables under consideration as inputs to the correction algorithm.

	B_{abs}			B_{ATN}			$B_{abs}\backslash B_{ATN}$			Tr			SSA			AAE
	467 nm	528 nm	652 nm	467 nm	528 nm	652 nm	467 nm	528 nm	652 nm	467 nm	528 nm	652 nm	467 nm	528 nm	652 nm	
Min.	45.0	38.5	29.5	162.0	140.1	98.9	0.14	0.12	0.10	0.27	0.34	0.45	0.27	0.25	0.21	1.25
1st Qu.	125.4	99.9	64.8	473.7	413.3	296.5	0.22	0.20	0.18	0.55	0.60	0.70	0.50	0.47	0.44	1.52
Median	216.5	169.5	112.1	843.9	721.8	528.5	0.25	0.23	0.21	0.66	0.71	0.79	0.72	0.72	0.70	1.72
Mean	320.2	245.9	160.2	1276.7	1091.0	781.6	0.26	0.24	0.22	0.68	0.72	0.79	0.66	0.66	0.65	1.99
3rd Qu.	407.5	316.2	203.7	1658.2	1418.6	1000.9	0.30	0.27	0.25	0.80	0.83	0.88	0.84	0.84	0.84	2.34
Max.	2370.9	1689.2	1295.8	11227.0	9280.7	6391.2	0.45	0.43	0.40	1.00	1.00	1.00	0.95	0.96	0.97	4.07

Figure S1 shows the relationships between $\frac{B_{abs}}{B_{ATN}}$ and each independent variable. It is clear that $\frac{B_{abs}}{B_{ATN}}$ increases with decreasing Tr, SSA, and AAE. However, the relationships are nonlinear, and the data points scatter fairly widely. Moreover, $\frac{B_{abs}}{B_{ATN}}$ spans a wide range of values at a single value of Tr, which inspired us to investigate the interactions among Tr, SSA, and AAE.

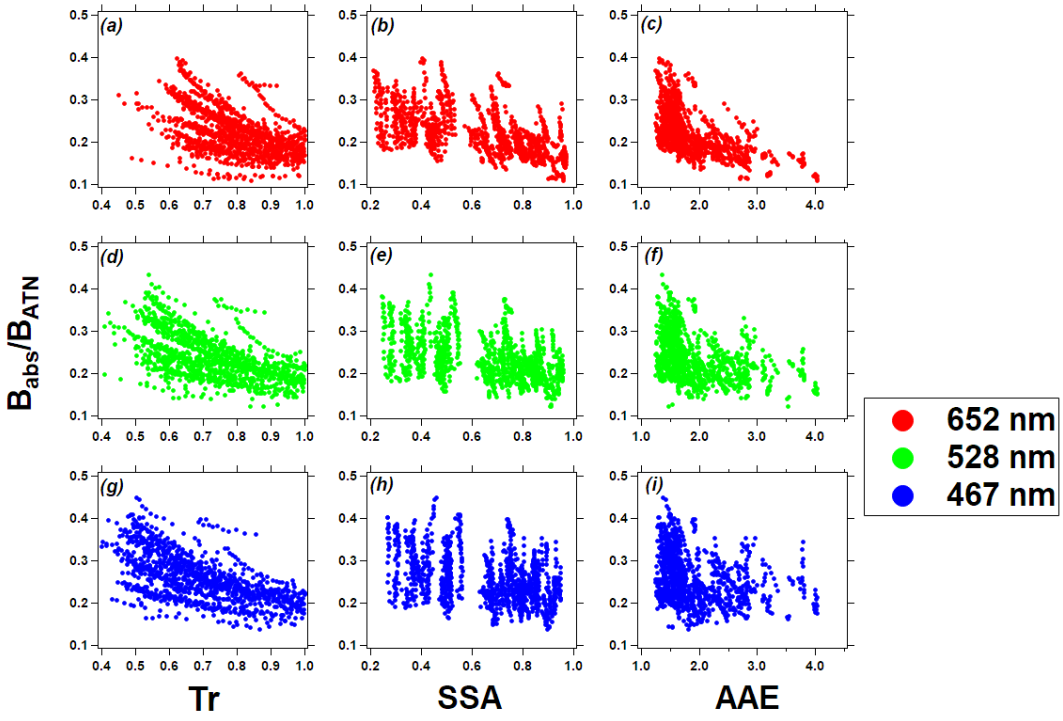

Figure S1. Scatter plot of $\frac{B_{abs}}{B_{ATN}}$ against Tr, SSA, and AAE at 652 nm, 528 nm, and 467 nm.

- *Prediction of $\frac{B_{abs}}{B_{ATN}}$ using multiple regression models*

Independent variables of $\frac{\mathrm{B_{abs}}}{\mathrm{B_{ATN}}}$ were identified by "best subset regression" (using both adjusted R^2 and Mallow's Cp as the criterion) and "stepwise regression" (both forward and backward). Variables tested for significance included Tr, SSA, AAE, and three-way interactions (Tr: SSA, SSA: AAE, Tr: AAE, and Tr: SSA: AAE). Regardless of wavelength, the best-subset models selected the same form of regression, which included all independent variables and the intercept (Table S2). However, the stepwise regression models varied across wavelengths: at 652 nm, the forward stepwise model was same as the best-subset models, but the backward stepwise model dropped two variables (Tr: AAE and Tr: SSA: AAE); at 528 nm and 467 nm, forward and backward stepwise regression produced the same model at each wavelength, but the selected variables were different at different wavelengths (see Table S2). Generally, the adjusted R^2 of best-subset models was greater or equal to the adjusted R^2 of stepwise models at each wavelength. As we placed a higher priority on prediction accuracy of $\frac{\mathrm{B_{abs}}}{\mathrm{B_{ATN}}}$, we selected the models that result in the greatest adjusted R^2 (the model including seven predictors).

Table S2 Predictors of $\frac{\mathrm{B_{abs}}}{\mathrm{B_{ATN}}}$ using "best subset regression" and "stepwise regression".

	652 nm			528 nm		467 nm	
	Best subset	**Stepwise (forward)**	**Stepwise (backward)**	**Best subset**	**Stepwise [a]**	**Best subset**	**Stepwise [a]**
R^2	0.620	0.620	0.607	0.544	0.510	0.531	0.531
Intercept	1.08±0.15	1.08±0.15	0.84±0.03	1.21±0.15	0.84±0.03	1.39±0.16	1.39±0.16
	***	***	***	***	***	***	***
Tr	-0.75±0.19	-0.75±0.19	-0.45±0.03	-0.89±0.20	-0.37±0.03	-1.12±0.23	-1.12±0.23
	***	***	***	***	***	***	***
SSA	-0.86±0.15	-0.86±0.15	-0.53±0.04	-0.89±0.15	-0.46±0.04	-1.07±0.17	-1.07±0.17
	***	***	***	***	***	***	***
AAE	-0.30±0.10	-0.30±0.10	-0.15±0.02	-0.44±0.10	-0.20±0.02	-0.57±0.11	-0.57±0.11
	**	**	***	***	***	***	***
Tr: SSA	0.79±0.19	0.79±0.19	0.38±0.04	0.77±0.21	0.17±0.04	0.99±0.25	0.99±0.25
	***	***	***	***	***	***	***
SSA: AAE	0.31±0.11	0.31±0.11	0.13±0.02	0.47±0.11	0.20±0.02	0.64±0.12	0.64±0.12
	**	**	***	***	***	***	***
Tr: AAE	0.19±0.13	0.19±0.13		0.34±0.14		0.51±0.16	0.51±0.16
	·	·		*		**	**
Tr: SSA: AAE	-0.24±0.13	-0.24±0.13		-0.38±0.14		-0.59±0.17	-0.59±0.17
	·	·		**		***	***
*** $p < 0.001$; ** $p < 0.01$; * $p < 0.05$; · $p < 0.1$.							

[a] At 528 nm and 467 nm, forward and backward stepwise approaches output the same regression model.

- *Transformation of the regression models*

A nonlinear transformation of variables is commonly used if a non-linear relationship exists between the independent and dependent variables (e.g., (Benoit, 2011; Creamer et al., 1989; Lek et al., 1996)). As seen in the first column in Fig. S1, there appears to be a logarithmic relationship between $\frac{B_{abs}}{B_{ATN}}$ and Tr, implying that logarithmic transformation of the regression model likely improve the performance of the regression model. We tried nonlinear transformation of the dependent variable. The results generally did not improve the regression results (the adjusted R^2 is smaller or equal to that of the original model); therefore, the original $\frac{B_{abs}}{B_{ATN}}$ was retained. Then, we transformed the dependent variables. Using ln(Tr) instead of Tr in the models improved the adjusted R^2 from 0.54 to 0.57 (528 nm) and from 0.53 to 0.58 (467 nm), but no improvement at 652 nm. Moreover, ln(Tr) has a physical meaning in that ln(Tr) = -ATN, so the transformed results are easy to interpret. Consequently, we adopted ln(Tr) in the regression model. No improvement was found using the transformation of SSA and AAE; therefore, the original SSA and AAE were retained. We present the results of the regression models using logarithmic transformation of Tr in Table S3.

Table S3 Predictors of $\frac{B_{abs}}{B_{ATN}}$ (similar to Table S2, but using ln(Tr) instead of Tr in the model).

	652 nm	**528 nm**	**467 nm**
R^2	0.62	0.57	0.58
Intercept	0.36±0.04	0.34±0.06	0.30±0.07
	***	***	***
ln(Tr)	-0.61±0.15	-0.73±0.14	-0.87±0.15
	***	***	***
SSA	-0.09±0.04	-0.14±0.06	-0.11±0.07
	*	*	·
AAE	-0.12±0.03	-0.11±0.04	-0.06±0.05
	***	**	·
ln(Tr): SSA	0.61±0.15	0.60±0.14	0.73±0.16
	***	***	***
SSA: AAE	0.09±0.03	0.09±0.04	0.06±0.03
	**	*	·
ln(Tr): AAE	0.19±0.10	0.33±0.10	0.45±0.10
	·	***	***
ln(Tr): SSA: AAE	-0.22±0.11	-0.36±0.10	-0.49±0.11
	*	***	***
*** $p < 0.001$; ** $p < 0.01$; * $p < 0.05$; · $p < 0.1$.			

- *Assessment of the fit of regression models*

After selecting the model, we performed "F-test" to determine whether the model with fewer variables predicted $\frac{B_{abs}}{B_{ATN}}$ better than the model with all predictors. The F-tests indicated that dropping any predictor did not improve the fit of the model (F-ratios >> 1 and P-value < 0.05).

We then analyzed the residuals of the selected model to test the adequacy of prediction. We found that the residuals were well scattered in a random pattern against ln(Tr), SSA and AAE (Fig. S2), indicating that the models as presented in Eq. (9) in the main text give the best accuracy.

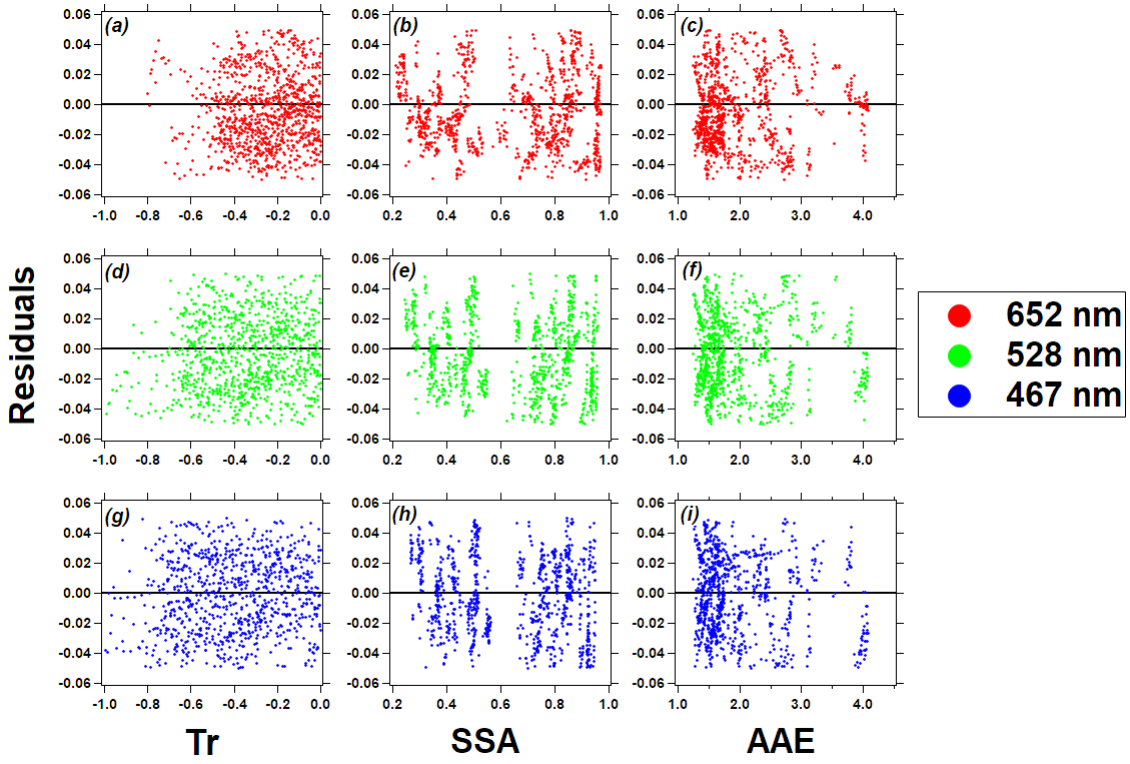

Figure S2. Scatter plot of residuals against Tr, SSA, and AAE at 652 nm, 528 nm, and 467 nm.

The above analyses were then repeated for TAP-related observations. The results were consistent with what we have found on the CLAP data. We present the final regression models to predict $\frac{B_{abs}}{B_{ATN}}$ for these TAP-related observations in Table S4.

Table S4 Predictors of $\frac{B_{abs}}{B_{ATN}}$ for TAP-related observations

	652 nm	**528 nm**	**467 nm**
R^2	0.36	0.32	0.35
Intercept	0.03±0.11	0.02±0.12	0.16±0.11
ln(Tr)	-1.20±0.39	-0.97±0.33	-0.53±0.28
	**	**	*
SSA	0.48±0.11	0.40±0.12	0.25±0.12
	***	***	*
AAE	0.20±0.07	0.18±0.08	0.10±0.08
	**	*	
ln(Tr): SSA	1.43±0.41	0.99±0.34	0.49±0.29
	***	**	.
SSA: AAE	-0.28±0.08	-0.23±0.08	-0.15±0.08

	***	**	.
ln(Tr): AAE	0.55±0.26	0.44±0.23	0.18±0.13
	*	*	
ln(Tr): SSA: AAE	-0.62±0.28	-0.47±0.24	-0.20±0.20
	*	*	
*** p < 0.001; ** p < 0.01; * p < 0.05; · p < 0.1.			

- *Interpretation of the regression models*

We can order the terms in Eq. (9) into two groups, the first group (terms that do not contain ln(Tr): $(G_0 + G_2 \times SSA(\lambda) + G_3 \times AAE + G_5 \times SSA(\lambda) \times AAE)$) defines the intercept on a graph of $\frac{B_{abs}}{B_{ATN}}$ against ln(Tr); the second group (all terms that contain the ln(Tr): $\ln(Tr(\lambda)) \times (G_1 + G_4 \times SSA(\lambda) + G_6 \times AAE + G_7 \times SSA(\lambda) \times AAE)$) defines the simple slope of the line (Dawson and Richter, 2006; Zedeck, 1971). As in this form, the new correction equation can be interpreted as following:

1. For a given wavelength, the relation between ln(Tr) and $\frac{B_{abs}}{B_{ATN}}$ varies across levels of SSA and AAE, and the combination of SSA and AAE.
2. Under different conditions of SSA and AAE, the same value of ln(Tr) may lead to various ratios between B_{abs} and B_{ATN}, and the compensation and/or reduction of B_{ATN} will be different to agree with the reference B_{abs}.

We also conduct simple slope analyses to explore the nature of the three-way interaction terms (Aiken et al., 1991). Specifically, we arbitrary assume four combinations of AAE and SSA: (1). SSA=0.95 and AAE=4; (2). SSA=0.8 and AAE=3; (3). SSA=0.8 and AAE=1.5; (4). SSA=0.4 and AAE=1. As seen in Fig. S3 (528 nm as an example), the $\frac{B_{abs}}{B_{ATN}}$-ln(Tr) relationship is moderated by different combinations of AAE and SSA. For example, the slope of "Comb. 4" in Fig. S3(b) is significantly different ($p<0.05$) from the slopes of other three combinations of SSA and AAE. Moreover, the intercept of the four lines are inconsistent, indicating that even when the filter is slightly loaded ($\ln(Tr) \longrightarrow 0$), the correction of B_{ATN} should be different for the aerosols with various optical properties.

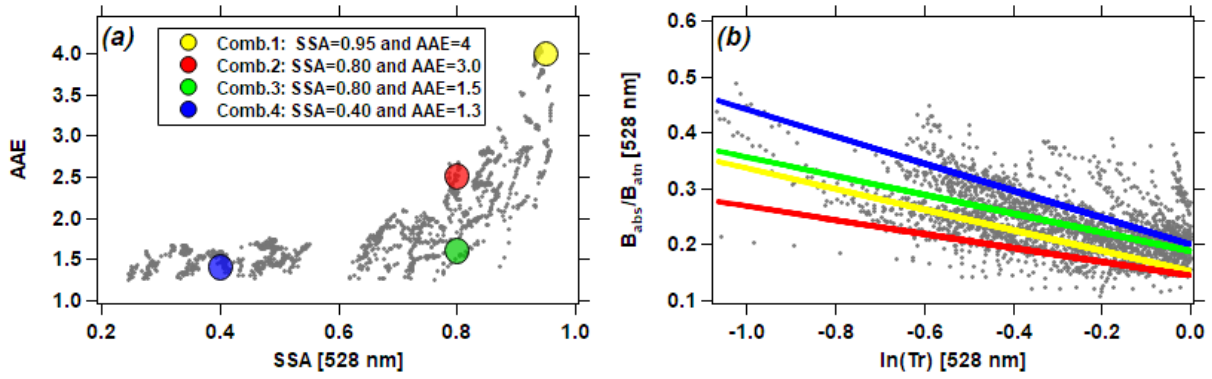

Figure S3. Simple slopes analysis of cross-level interaction of SSA and AAE in predicting $\frac{B_{abs}}{B_{ATN}}$ as a function of ln(Tr) at 528 nm.

Fig. S4 compares the simulated "g" term from our correction and the previous corrections. In panels S4a and S4b, we use the original coefficients reported in B1999 and V2005 to simulate the "g" term in Eq. 8. In panels S4c and S4d, we use the updated B1999 and V2005 coefficients from our Table S7 (FIREX-CLAP). When simulating Eq. 9 (panel S4e), we estimate AAE as a function of SSA (AAE = a + b×SSA^c), similar to the procedure of "Algorithm C" in our manuscript. Then, we plot the results of "g" derived by all corrections as a function of SSA (panels S4f – S4h: Tr = 0.9, 0.75, and 0.5).

In general, the values of "g" term from all corrections increase with decreasing Tr and SSA. However, the figure suggests that there are variations among the corrections for different combinations of Tr and SSA. For example, the original B1999 and V2005 corrections tend to yield greater values of "g" than the other corrections (eventually, insufficient correction), and the agreement between them gets worse as Tr and SSA decrease (panels S4f - S4h). Another observation from the figure is that our correction is in better agreement with the updated B1999 and V2005, but this agreement depends on both SSA and Tr. For example, when SSA > 0.95, our correction does not exhibit as strong of a non-linearity as the updated B1999 and V2005.

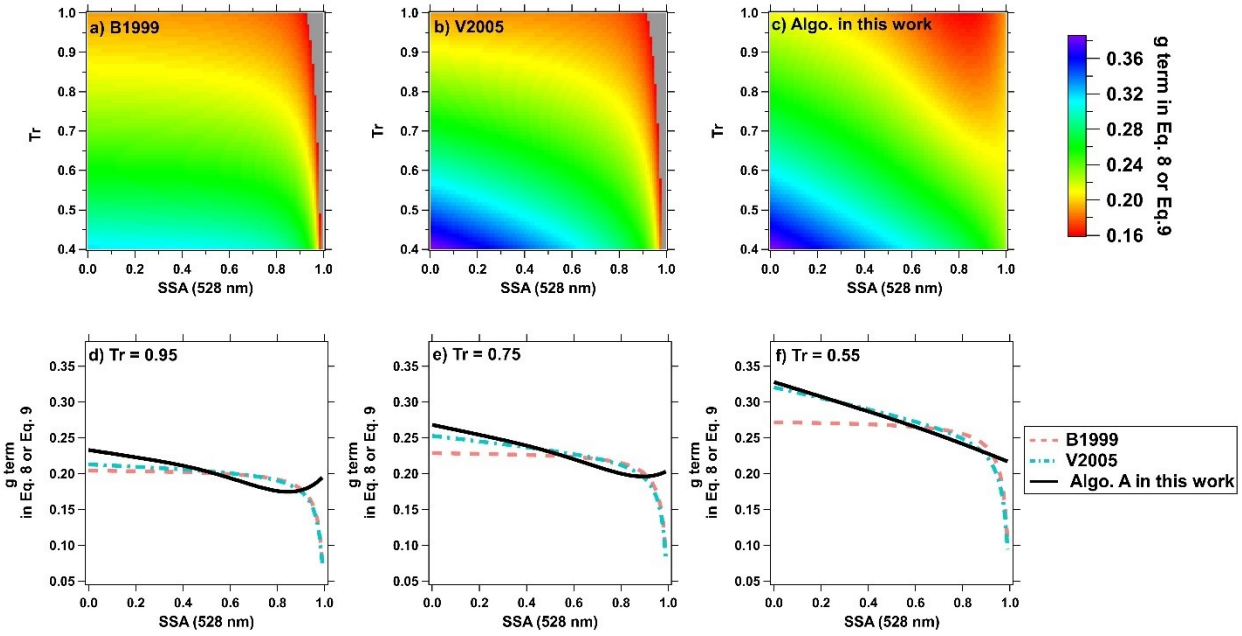

Figure S4. Simulated "g" term (528 nm) in Eq. (8) or Eq. (9). In panel c) and d), the grey regions correspond to "g" values less than 0.15.

2. Comparison of the corrections against different parameters

To further investigate how different algorithms apply to different aerosol properties, we generated Figures S5 and S6 (SGP and FIREX, respectively), in which the variable on y axis is B_{abs} ratio = corrected B_{abs} (different corrections) / B_{abs} from photoacoustic instruments (reference), and the parameters on x axis include relative humidity (RH), AAE, SAE, and SSA (528 nm). In general, an apparent association between the B_{abs} ratio and these parameters exists in the uncorrected data (raw B_{ATN}), and this association persists when using B1999 and V2005, especially for RH and SSA. However, these associations are reduced or eliminated when applying our algorithm on the

filter-based absorption measurements. Although RH and SAE are not included in our algorithm, our algorithm appears to account for any influence that these parameters have on the measurements.

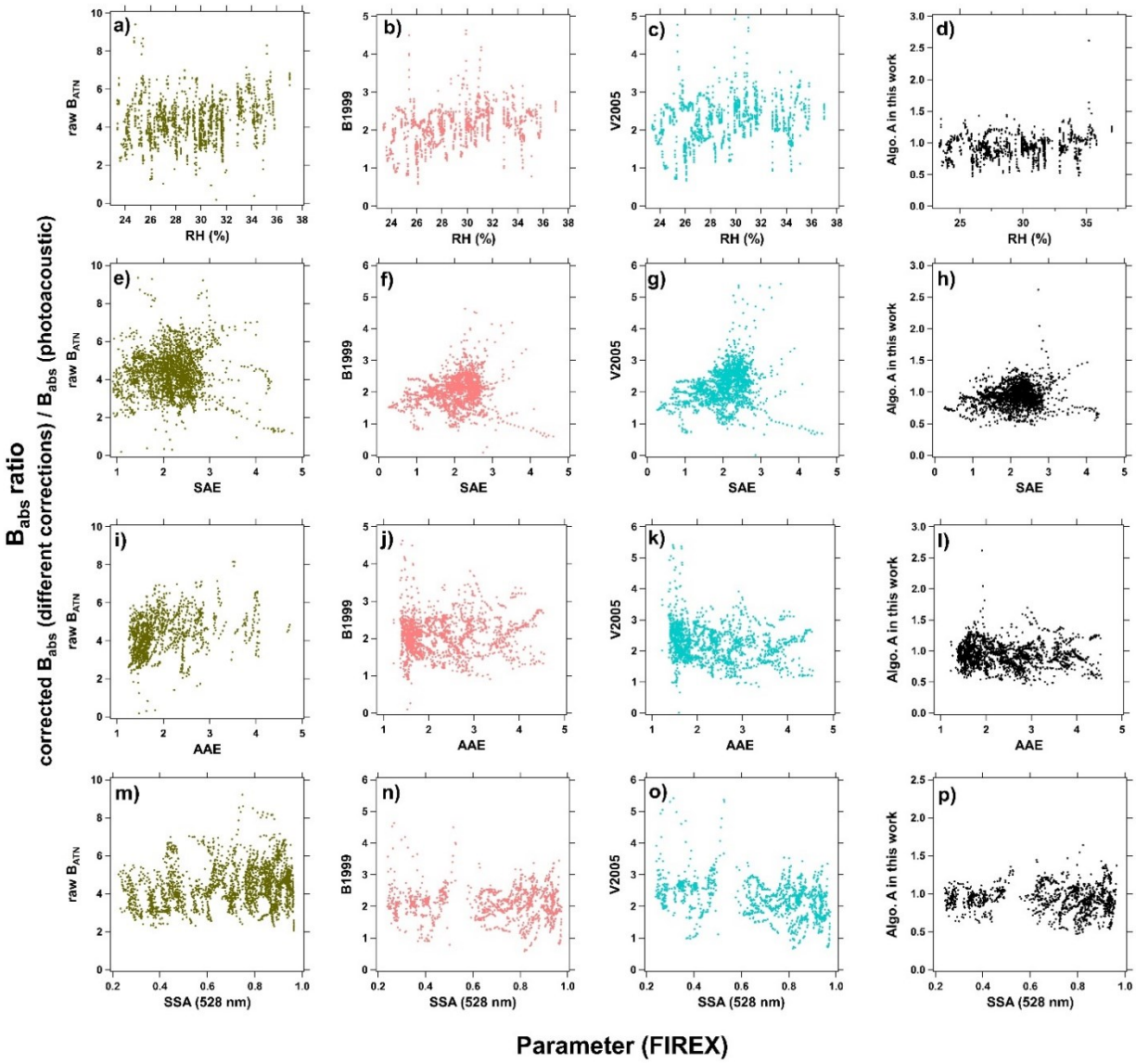

Figure S5. B_{abs} ratio vs. different aerosol properties from the FIREX campaign. In the first column, B_{abs} ratio = uncorrected B_{ATN} / B_{abs} (photoacoustic). In the other columns, B_{abs} ratio = corrected B_{abs} from different corrections / B_{abs} (photoacoustic).

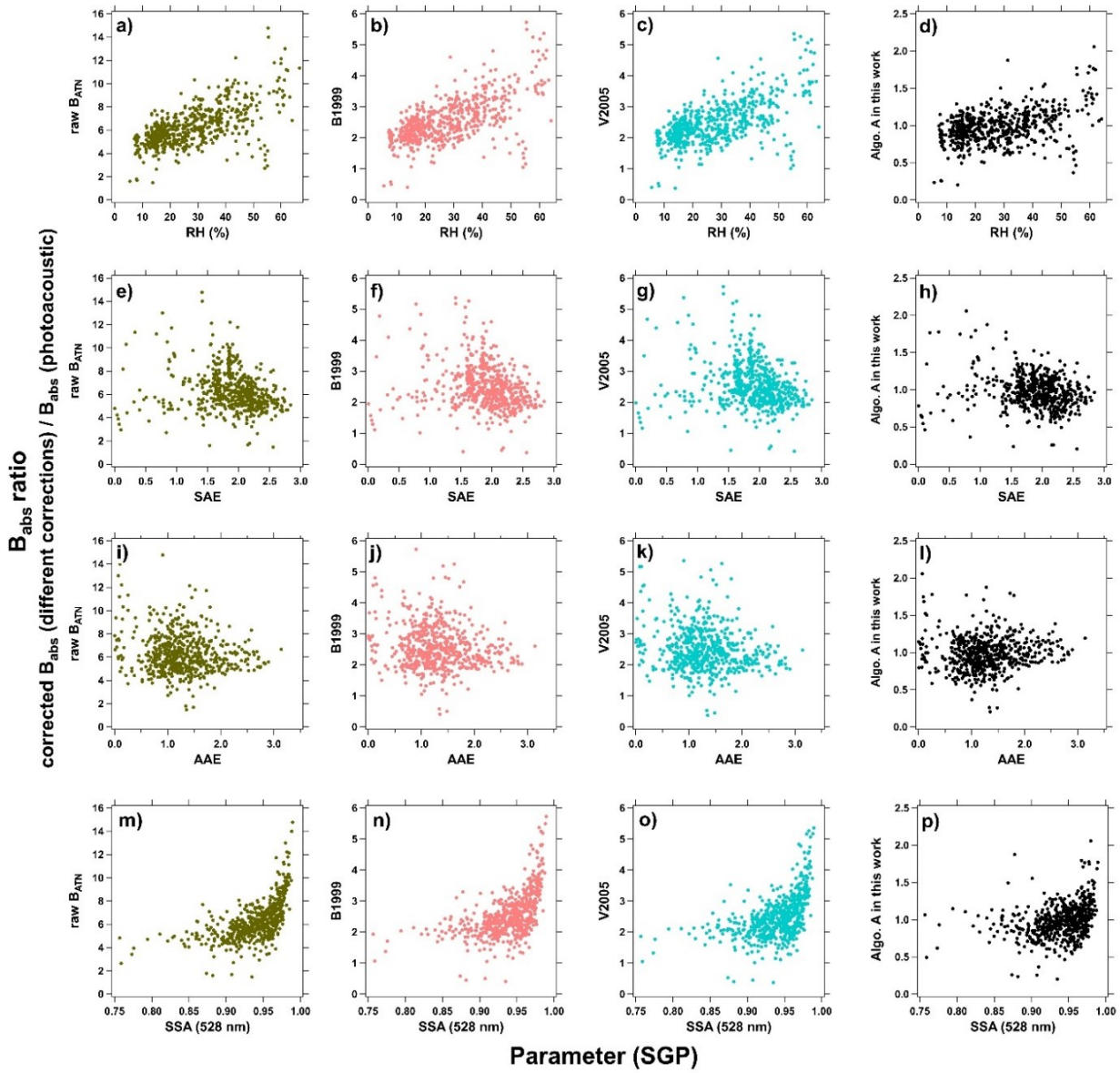

Figure S6. B_{abs} ratio vs. different parameters at the SGP site. In the first column, B_{abs} ratio = uncorrected B_{ATN} / B_{abs} (photoacoustic). In the other columns, B_{abs} ratio = corrected B_{abs} by different corrections / B_{abs} (photoacoustic).

We also investigated how number-based geometric mean diameter (d_{pg}) of aerosols affects the corrections' performance. Arguably, the pattern for the B1999 and V2005 data agrees with those reported in Moteki et al. (2010) and Nakayama et al. (2010), in that absorption tends to be over-estimated for smaller particles and that this effect is gradually reduced with increasing particle size. Unfortunately, the size distribution of SGP aerosols is unavailable during our target time period, so we cannot extend this analysis to those data.

Compared to B1999 and V2005, the B_{abs} ratio derived by our new correction is much close to unity when plotting against d_{pg}. Although d_{pg} was not considered when developing the algorithm, any effects related to particle size appear to be captured by our algorithm, potentially in one of the

interaction terms (like RH and SAE were above). Unfortunately, we do not have a strong qualitative physical explanation for this.

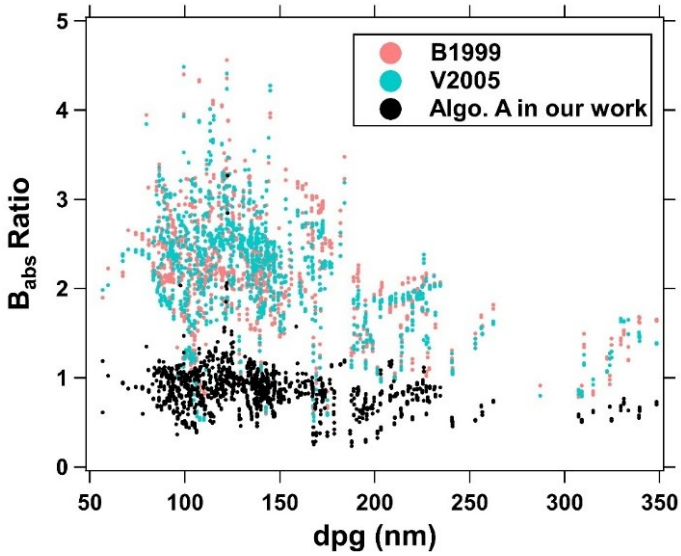

Figure S7. B_{abs} ratio vs. d_g from the FIREX campaign.

3. Application of the CTS correction algorithm on SGP aerosols

We applied the constrained two-stream (CTS) correction proposed in Müller et al. (2014) our SGP-CLAP data. The parameters used by us (e.g., δ_{af}, δ_{sf}, μ_1, χ) are the same as those in Müller et al. (2014) and Davies et al. (2019). We first regenerate Fig. 6 and Fig. 7 in Müller et al. (2014) to validate our coding (see Fig. S8 below).

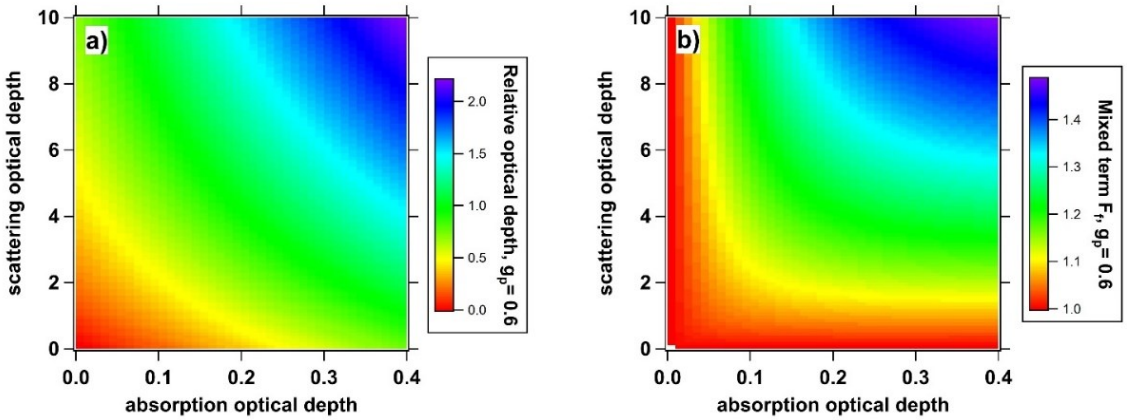

Figure S8. Simulated relative optical depth (panel a) and F_f (panel b) as a function of scattering and absorption optical depths.

As seen in Figure S9, B_{abs} corrected by the M2014 correction agrees fairly well with those derived by the original B1999 and V2005, but overestimates the photoacoustic measurements by factors ~2.5. Another observation is that the performance of M2014 increases as the wavelength decreases that (as seen by the R^2), which is consistent with the results for urban emissions in Davies et al. (2019).

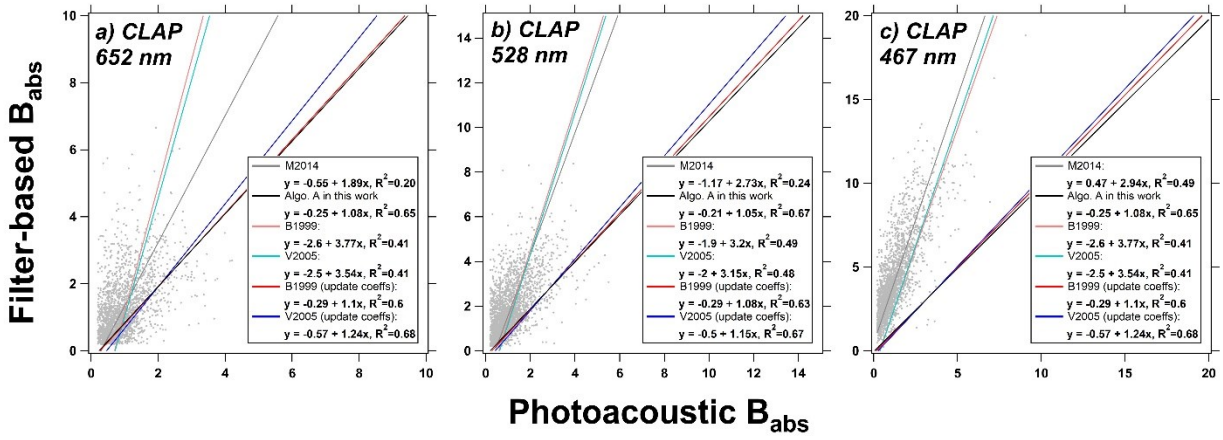

Figure S9. Inter-comparison between the CLAP-derived B_{abs} corrected by the M2014 correction and the reference B_{abs} at 652, 528, and 467 nm for the SGP data. The relationships derived by the other corrections discussed in our manuscript are given in the figure.

4. The procedure for simulating the uncertainty of the new algorithms in Section 3.5

The simulation is performed in seven steps:

1. We arbitrarily set concentration ranges of "true" B_{abs} at 652 nm from 100 to 2500 Mm^{-1} and AAE from 0.5 to 4.5 (number of cases = 500).
2. For each combination of "true" B_{abs} at 652 nm and AAE (500 × 500 in total), we calculate the B_{abs} at 528 and 467 nm. For example, B_{abs} (467 nm) = B_{abs} (652 nm) × $(467/652)^{-AAE}$.
3. With the observed power relationship between AAE and SSA (similar to Fig. 6 in the main text, but using B_{abs} instead of B_{ATN} as the absorption measurements), we compute SSA for each AAE value. The derived SSA is then used to calculate B_{scat} (B_{scat} = SSA/(1-SSA)× B_{abs}).
4. With the observed relationship between B_{abs} and B_{ATN} (Fig. 3 in the main text), we calculate the filter-based B_{ATN} at all three wavelengths.
5. We simulate the measurements of filter-based B_{ATN}, photoacoustic B_{abs}, and NEPH-derived B_{scat} by adding the measurement uncertainty of the instruments to the parameters described in Steps 1-4. The measurement uncertainties are forms of normal distribution (Table 1 in the main text). Figure S4 shows an example of a dataset derived by Steps 1-5.
6. We implement "Algorithm B" on the derived dataset from Step 5. The corrected filter-based results are then compared to the "true" B_{abs}.
7. The above procedure is repeated 1000 times using a Monte Carlo simulation to evaluate bias and power of our correction algorithms.

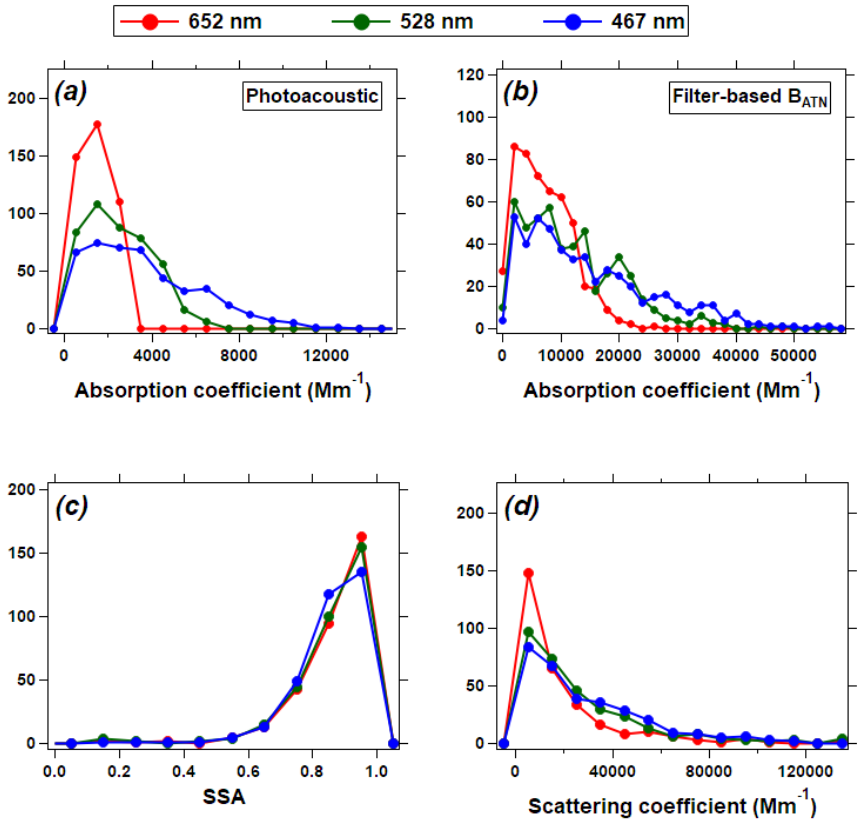

Figure S10. Distribution of the simulated measurements derived by Steps 1-5 in the above procedure.

SUPPLEMENTARY TABLES

Table S5 Relationship between the filter-based B_{abs} (FIREX-TAP and SGP-PSAP) corrected by B1999 and V2005 algorithms and the reference B_{abs} at 652, 528, and 467 nm. This table complements Table 3 from in the main text.

		652 nm	528 nm	467 nm
FIREX -TAP	**B1999**	y = -46 + 2.17x (0.83)	y = -55 + 1.88x (0.85)	y = -61 + 1.75x (0.86)
	V2005	y = -50 + 2.23x (0.85)	y = -62 + 2.03x (0.85)	y = -76 + 2.07x (0.86)
	B1999 (update coeffs)	y = -12 + 1.00x (0.85)	y = -17 + 1.00x (0.86)	y = -19 + 0.99x (0.87)
	V2005 (update coeffs)	y = -13 + 1.02x (0.87)	y = -16 + 1.00x (0.87)	y = -16 + 0.99x (0.87)
SGP -PSAP	**B1999**	y = -6.40 + 5.86x (0.32)	y = -5.24 + 4.47(0.43)	y = -4.10 + 3.88x (0.51)
	V2005	y = -7.10 + 6.10x (0.32)	y = -6.72 + 5.11x (0.40)	y = -5.43 + 5.43x (0.49)
	B1999 (update coeffs)	y = -0.52 + 1.21x (0.40)	y = -0.57 + 1.18x (0.50)	y = -0.37 + 1.09x (0.55)
	V2005 (update coeffs)	y = -0.89 + 1.40x (0.46)	y = -0.76 + 1.24x (0.52)	y = -0.45 + 1.11x (0.58)

Table S6 Inter-comparison between different filter-based B_{abs} corrected by the same algorithm. The value in the bracket represents the coefficient of determination (R^2) of the linear relationship.

		FIREX: CLAP vs. TAP	SGP: CLAP vs. PSAP
B1999	**652 nm**	y = 7.00 + 1.29x (0.91)	y = 0.61 + 0.77x (0.57)
	528 nm	y = 13.61 + 1.36x (0.90)	y = 1.09 + 0.78x (0.53)
	467 nm	y = 25.40 + 1.30x (0.89)	y = 1.61 + 0.75x (0.55)
V2005	**652 nm**	y = 4.42 + 1.33x (0.90)	y = 0.87 + 0.68x (0.54)
	528 nm	y = 12.07 + 1.40x (0.89)	y = 1.39 + 0.69x (0.53)
	467 nm	y = 28.84 + 1.32x (0.88)	y = 1.85 + 0.68x (0.56)
B1999 (update coeffs)	**652 nm**	y = 4.20 + 1.01x (0.88)	y = 0.01 + 0.96x (0.61)
	528 nm	y = 8.02 + 1.01x (0.86)	y = 0.16 + 0.91x (0.65)
	467 nm	y = 13.18 + 1.01x (0.85)	y = 0.21 + 0.90x (0.70)
V2005 (update coeffs)	**652 nm**	y = 3.30 + 1.02x (0.89)	y = 0.08 + 0.92x (0.68)
	528 nm	y = 6.81 + 1.01x (0.87)	y = 0.18 + 0.90x (0.68)
	467 nm	y = 11.00 + 1.01x (0.85)	y = 0.24 + 0.90x (0.72)

Table S7 Updated coefficients in the B1999 and V2005 algorithms using our data [a].

				C2	C3	C1		
B1999 [b]	FIREX	CLAP	652 nm	3.42	2.00	0.016		
			528 nm	3.47	1.77	0.016		
			467 nm	3.49	1.43	0.016		
		TAP	652 nm	1.58	2.13	0.016		
			528 nm	1.19	2.07	0.016		
			467 nm	1.11	1.93	0.016		
	SGP	CLAP	652 nm	-1.39	6.12	0.016		
			528 nm	0.88	4.03	0.016		
			467 nm	1.51	3.46	0.016		
		PSAP	652 nm	1.730	3.930	0.016		
			528 nm	2.230	3.180	0.016		
			467 nm	2.590	2.940	0.016		
				C4	C5	C6	C7	C1
V2005 [c]	FIREX	CLAP	652 nm	0.19	-0.34	0.90	-0.83	0.022
			528 nm	0.19	-0.23	0.95	-0.50	0.017
			467 nm	0.20	-0.19	0.95	-0.15	0.015
		TAP	652 nm	0.28	-0.44	0.88	-1.07	0.022
			528 nm	0.31	-0.36	0.94	-0.94	0.017
			467 nm	0.32	-0.35	0.92	-0.79	0.015
	SGP	CLAP	652 nm	0.22	-1.22	1.14	-1.22	0.022
			528 nm	0.20	-0.94	1.07	-1.09	0.017
			467 nm	0.20	-0.78	1.01	-0.99	0.015
		PSAP	652 nm	0.19	-0.55	0.98	-0.92	0.022
			528 nm	0.19	-0.48	1.00	-0.90	0.017
			467 nm	0.18	-0.44	0.96	-0.84	0.015

[a] We update the coefficients in B1999 and V2005 using the Levenberg-Marquardt algorithm (Levenberg, 1944), which is different from the original approach to fitting the coefficients in those papers. Specifically, we hold C_1 to be the same as the value in B1999 and V2005 and iteratively fit the other coefficients until the chi-square of the coefficients are minimized.

[b] The general form of the B1999 algorithm: $B_{abs} = B_{ATN} \times \frac{1}{C_2 \times Tr + C_3} - C_1 \times B_{scat}$

[c] The general form of the V2005 algorithm: $B_{abs} = B_{ATN} \times C_4 + C_5 \times (C_6 + C_7 \times SSA) \times \ln(Tr) - C_1 \times B_{scat}$

Table S8 Updated coefficients in the B1999 algorithm using different subsets of AAE and SSA for the FIREX measurements. The aerosols with different subranges of AAE and SSA result in different values of C2 and C3 for different wavelengths, which are different from the "default" values in B1999. The blank cells represent combinations with no available data.

					SSA							SSA		
CLAP	C2		wavelength	<0.4	0.4-0.8	0.8-1	TAP	C2		wavelength	<0.4	0.4-0.8	0.8-1
	AAE	<1.8	652 nm	4.384	3.249			AAE	<1.8	652 nm	3.419	1.917	
			528 nm	3.988	3.395					528 nm	3.196	1.929	
			467 nm	3.778	3.132					467 nm	2.954	1.895	
		1.8-3.4	652 nm		3.312	1.583			1.8-3.4	652 nm		1.355	-3.209
			528 nm		4.150	2.656				528 nm		2.462	-1.184
			467 nm		3.982	2.576				467 nm		2.761	-0.330
		>3.4	652 nm			3.908			>3.4	652 nm			0.992
			528 nm			3.800				528 nm			1.212
			467 nm			3.619				467 nm			1.537
	C3		wavelength	<0.4	0.4-0.8	0.8-1		C3		wavelength	<0.4	0.4-0.8	0.8-1
	AAE	<1.8	652 nm	0.623	2.049			AAE	<1.8	652 nm	0.101	2.098	
			528 nm	0.960	1.664					528 nm	0.234	1.563	
			467 nm	0.941	1.619					467 nm	0.380	1.394	
		1.8-3.4	652 nm		2.726	4.085			1.8-3.4	652 nm		2.664	6.215
			528 nm		1.768	2.618				528 nm		1.228	3.791
			467 nm		1.733	2.143				467 nm		0.549	2.930
		>3.4	652 nm			1.881			>3.4	652 nm			3.503
			528 nm			1.199				528 nm			2.365
			467 nm			0.872				467 nm			1.835

Table S9 Updated coefficients in the V2005 algorithm using different subsets of AAE and SSA for the FIREX measurements. The aerosols with different subranges of AAE and SSA result in different values of C4 - C7 for different wavelengths, which are different from the "default" values in V2005. The blank cells represent combinations with no available data.

					SSA							SSA	
CLAP	C4		wavelength	<0.4	0.4-0.8	0.8-1	TAP	C4		wavelength	<0.4	0.4-0.8	0.8-1
	AAE	<1.8	652 nm	0.194	0.189			AAE	<1.8	652 nm	0.276	0.254	
			528 nm	0.197	0.189					528 nm	0.280	0.284	
			467 nm	0.204	0.200					467 nm	0.285	0.302	
		1.8-3.4	652 nm		0.169	0.184			1.8-3.4	652 nm		0.254	0.335
			528 nm		0.172	0.192				528 nm		0.280	0.376
			467 nm		0.173	0.210				467 nm		0.291	0.379
		>3.4	652 nm			0.191			>3.4	652 nm			0.245
			528 nm			0.202				528 nm			0.285
			467 nm			0.218				467 nm			0.297
	C5		wavelength	<0.4	0.4-0.8	0.8-1		C5		wavelength	<0.4	0.4-0.8	0.8-1
	AAE	<1.8	652 nm	-0.353	-0.225			AAE	<1.8	652 nm	-0.057	-0.075	
			528 nm	-0.384	-0.318					528 nm	-0.175	-0.365	
			467 nm	-0.362	-0.343					467 nm	-0.146	-0.507	
		1.8-3.4	652 nm		-0.070	-0.035			1.8-3.4	652 nm		-2.349	-1.234
			528 nm		0.188	-0.059				528 nm		-4.758	-0.740
			467 nm		-0.093	-0.489				467 nm		-1.298	0.224
		>3.4	652 nm			-0.277			>3.4	652 nm			0.202
			528 nm			-0.392				528 nm			-0.093
			467 nm			-0.216				467 nm			-0.216
	C6		wavelength	<0.4	0.4-0.8	0.8-1		C6		wavelength	<0.4	0.4-0.8	0.8-1

	AAE	<1.8	652 nm	0.795	0.852			AAE	<1.8	652 nm	-6.739	0.613	
			528 nm	0.861	0.880					528 nm	-0.605	0.945	
			467 nm	0.814	0.851					467 nm	-1.151	0.933	
		1.8-3.4	652 nm		1.026	1.038			1.8-3.4	652 nm		1.141	1.130
			528 nm		2.230	-0.327				528 nm		0.976	0.938
			467 nm		-2.056	0.979				467 nm		1.115	0.900
		>3.4	652 nm			1.071			>3.4	652 nm			0.750
			528 nm			1.094				528 nm			1.106
			467 nm			0.969				467 nm			1.004
	C7		wavelength	SSA				C7		wavelength	SSA		
				<0.4	0.4-0.8	0.8-1					<0.4	0.4-0.8	0.8-1
	AAE	<1.8	652 nm	-0.517	-0.579			AAE	<1.8	652 nm	41.858	0.725	
			528 nm	-1.016	-0.810					528 nm	8.037	-0.892	
			467 nm	-0.645	-0.784					467 nm	10.428	-1.052	
		1.8-3.4	652 nm		0.341	0.209			1.8-3.4	652 nm		-1.472	-1.474
			528 nm		-3.842	2.175				528 nm		-1.240	-1.238
			467 nm		4.561	-0.863				467 nm		-1.133	-0.904
		>3.4	652 nm			-0.631			>3.4	652 nm			-1.031
			528 nm			-0.691				528 nm			-0.248
			467 nm			0.044				467 nm			-0.487

Table S10 Updated coefficients in the B1999 algorithm using different subsets of AAE and SSA for the SGP measurements. The aerosols with different subranges of AAE and SSA result in different values of C2 and C3 for different wavelengths, which are different from the "default" values in B1999. The blank cells represent combinations with no available data.

CLAP	C2		wavelength	SSA			PSAP	C2		wavelength	SSA		
				<0.8	0.8-0.9	0.9-1					<0.8	0.8-0.9	0.9-1
	AAE	<1	652 nm	1.045	-1.532	3.071		AAE	<1	652 nm	3.887	-0.461	1.924
			528 nm	1.894	1.559	2.141				528 nm	4.164	-1.480	3.588
			467 nm	1.362	4.005	2.165				467 nm	4.627	0.858	1.154
		1-2	652 nm		0.110	-7.351			1-2	652 nm		1.186	1.376
			528 nm		1.966	-1.961				528 nm		2.555	2.338
			467 nm		2.069	0.175				467 nm		3.234	2.719
		>2	652 nm			-0.276			>2	652 nm			1.959
			528 nm			3.928				528 nm			1.989
			467 nm			2.900				467 nm			2.551
	C3		wavelength	SSA				C3		wavelength	SSA		
				<0.8	0.8-0.9	0.9-1					<0.8	0.8-0.9	0.9-1
	AAE	<1	652 nm	3.684	6.600	3.825		AAE	<1	652 nm	2.308	6.071	4.609
			528 nm	3.165	4.198	4.612				528 nm	2.072	6.907	3.571
			467 nm	3.751	2.258	4.735				467 nm	2.081	5.358	5.217
		1-2	652 nm		5.480	12.699			1-2	652 nm		4.761	5.033
			528 nm		3.667	7.489				528 nm		3.367	3.849
			467 nm		3.592	5.476				467 nm		3.031	3.515
		>2	652 nm			6.255			>2	652 nm			4.939
			528 nm			1.805				528 nm			3.747
			467 nm			2.551				467 nm			3.212

Table S11 Updated coefficients in the V2005 algorithm using different subsets of AAE and SSA for the SGP measurements. The aerosols with different subranges of AAE and SSA result in different values of C4 - C7 for different wavelengths, which are different from the "default" values in V2005. The blank cells represent combinations with no available data.

	C4		wavelength	SSA		
				<0.8	0.8-0.9	0.9-1
CLAP	AAE	<1	652 nm	0.210	0.202	0.152
			528 nm	0.196	0.172	0.152
			467 nm	0.193	0.159	0.145
		1-2	652 nm		0.184	0.194
			528 nm		0.179	0.182
			467 nm		0.176	0.176
		>2	652 nm			0.172
			528 nm			0.176
			467 nm			0.182

	C5		wavelength	SSA		
				<0.8	0.8-0.9	0.9-1
CLAP	AAE	<1	652 nm	-0.596	-2.474	-2.370
			528 nm	-0.517	-1.512	-1.681
			467 nm	-0.571	-1.161	-1.102
		1-2	652 nm		-1.378	-3.306
			528 nm		-0.267	-1.799
			467 nm		-0.182	-1.509
		>2	652 nm			-2.253
			528 nm			1.733
			467 nm			-0.094

	C6		wavelength	SSA		
				<0.8	0.8-0.9	0.9-1
CLAP	AAE	<1	652 nm	0.922	1.027	1.204
			528 nm	0.943	1.403	1.242
			467 nm	0.922	1.125	0.998
		1-2	652 nm		1.183	1.276
			528 nm		0.965	1.215
			467 nm		0.952	1.104
		>2	652 nm			1.415
			528 nm			1.162
			467 nm			0.957

	C7		wavelength	SSA		
				<0.8	0.8-0.9	0.9-1
CLAP	AAE	<1	652 nm	-1.124	-1.216	-1.256
			528 nm	-1.084	-1.579	-1.313
			467 nm	-1.111	-1.194	-1.036
		1-2	652 nm		-1.371	-1.426
			528 nm		-0.862	-1.336
			467 nm		-0.718	-1.187
		>2	652 nm			-1.500
			528 nm			-1.335
			467 nm			0.065

	C4		wavelength	SSA		
				<0.8	0.8-0.9	0.9-1
PSAP	AAE	<1	652 nm	0.172	0.182	0.163
			528 nm	0.161	0.183	0.146
			467 nm	0.144	0.159	0.154
		1-2	652 nm		0.171	0.167
			528 nm		0.170	0.166
			467 nm		0.159	0.163
		>2	652 nm			0.157
			528 nm			0.178
			467 nm			0.174

	C5		wavelength	SSA		
				<0.8	0.8-0.9	0.9-1
PSAP	AAE	<1	652 nm	-0.805	0.611	-0.137
			528 nm	-0.624	0.133	-0.072
			467 nm	-0.986	-0.535	-0.049
		1-2	652 nm		-0.652	-0.008
			528 nm		-0.411	-0.084
			467 nm		-0.381	-0.032
		>2	652 nm			0.773
			528 nm			-0.094
			467 nm			-0.058

	C6		wavelength	SSA		
				<0.8	0.8-0.9	0.9-1
PSAP	AAE	<1	652 nm	1.024	0.865	0.977
			528 nm	1.002	0.569	1.116
			467 nm	1.036	0.921	0.870
		1-2	652 nm		0.949	1.289
			528 nm		0.973	1.025
			467 nm		0.937	0.976
		>2	652 nm			0.854
			528 nm			1.043
			467 nm			1.053

	C7		wavelength	SSA		
				<0.8	0.8-0.9	0.9-1
PSAP	AAE	<1	652 nm	-1.269	-0.994	-0.739
			528 nm	-1.096	-0.412	-0.317
			467 nm	-1.190	-1.019	-0.410
		1-2	652 nm		-1.025	2.107
			528 nm		-0.922	-0.477
			467 nm		-0.837	2.856
		>2	652 nm			-0.961
			528 nm			-0.548
			467 nm			0.088

Table S12 Computation of the quartile deviation for the derived coefficient values in Algorithm A using half of the CLAP observation. The box-and-whisker plots of the derived coefficient values are presented in Fig. S7.

	FIREX			**SGP**		
	652 nm	**528 nm**	**467 nm**	**652 nm**	**528 nm**	**467 nm**
G0	0.012	0.012	0.015	0.043	0.037	0.043
G1	0.057	0.047	0.049	0.428	0.333	0.309
G2	0.023	0.022	0.025	0.059	0.050	0.056
G3	0.008	0.009	0.010	0.035	0.029	0.032
G4	0.094	0.077	0.074	0.573	0.409	0.388
G5	0.013	0.013	0.015	0.050	0.041	0.042
G6	0.044	0.036	0.035	0.340	0.244	0.224
G7	0.068	0.036	0.054	0.460	0.334	0.285

SUPPLEMENTARY FIGURES

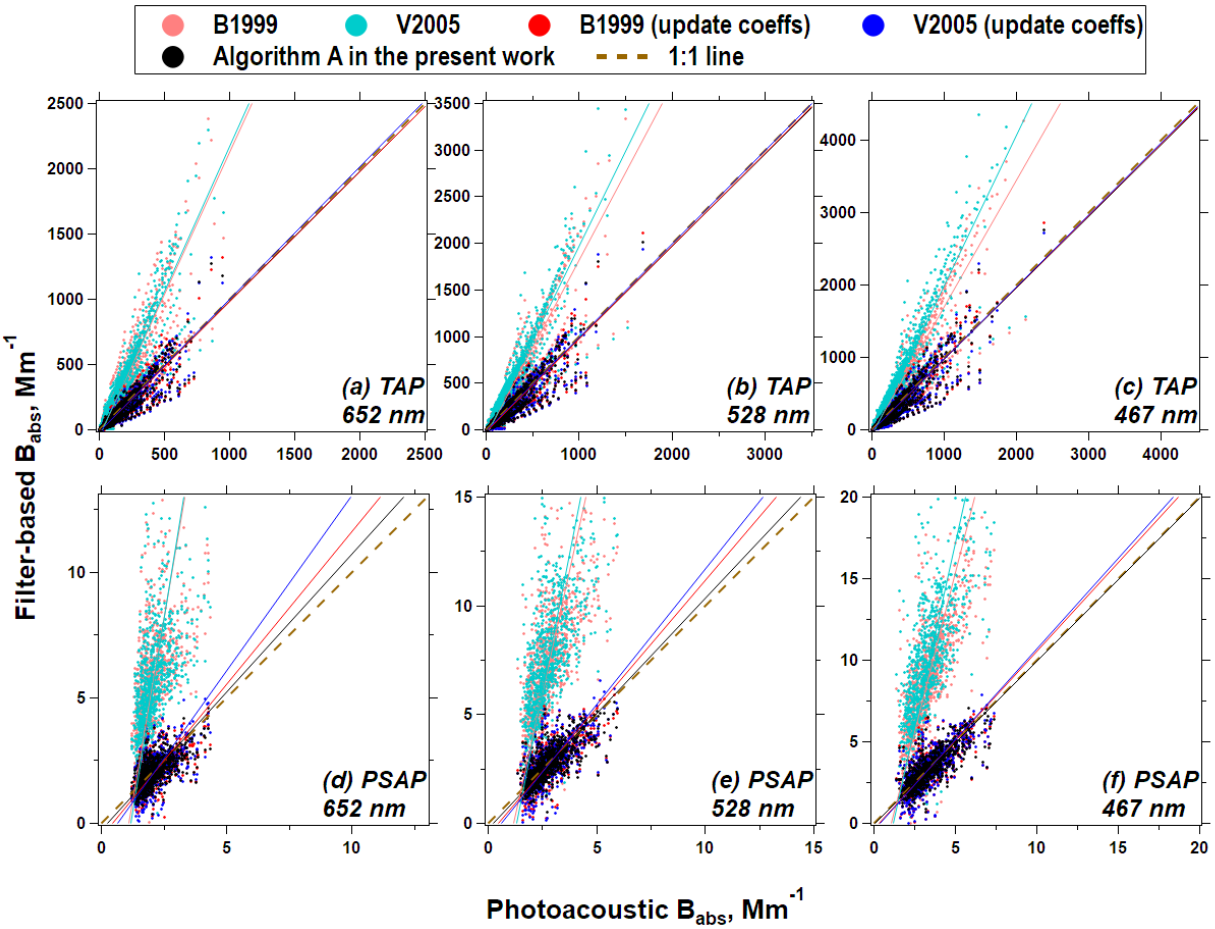

Figure S11. Inter-comparison between the filter-based B_{abs} (FIREX-TAP and SGP-PSAP) corrected by different algorithms and the reference B_{abs} at 652, 528, and 467 nm. The solid lines represent linear regressions, while the dashed line is a 1:1 line.

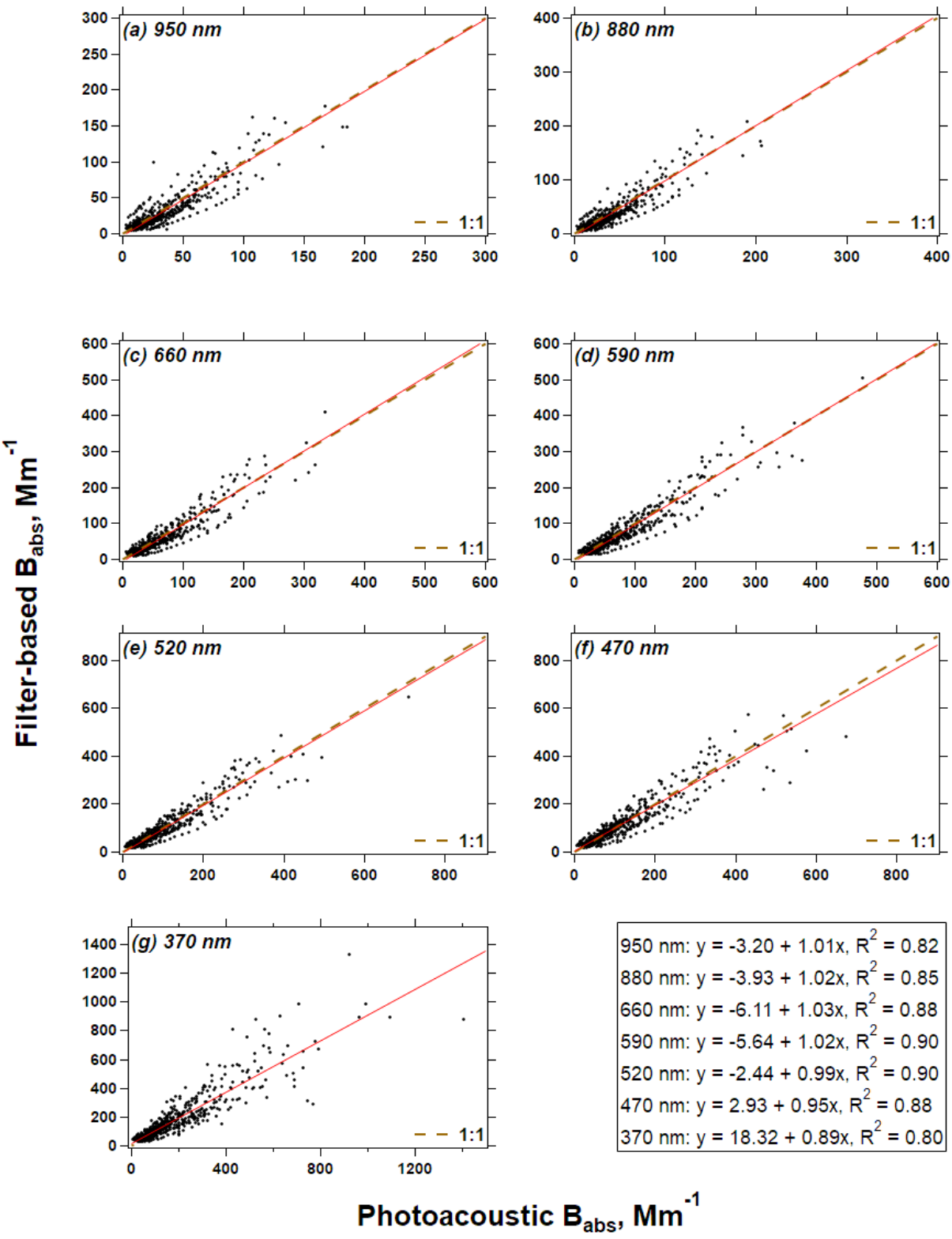

Figure S12. The AETH-derived B_{abs} (corrected by Algorithm A in the present work) versus photoacoustic B_{abs} for the FIREX aerosols. The solid lines represent a linear regression, while the dashed lines are 1:1 lines.

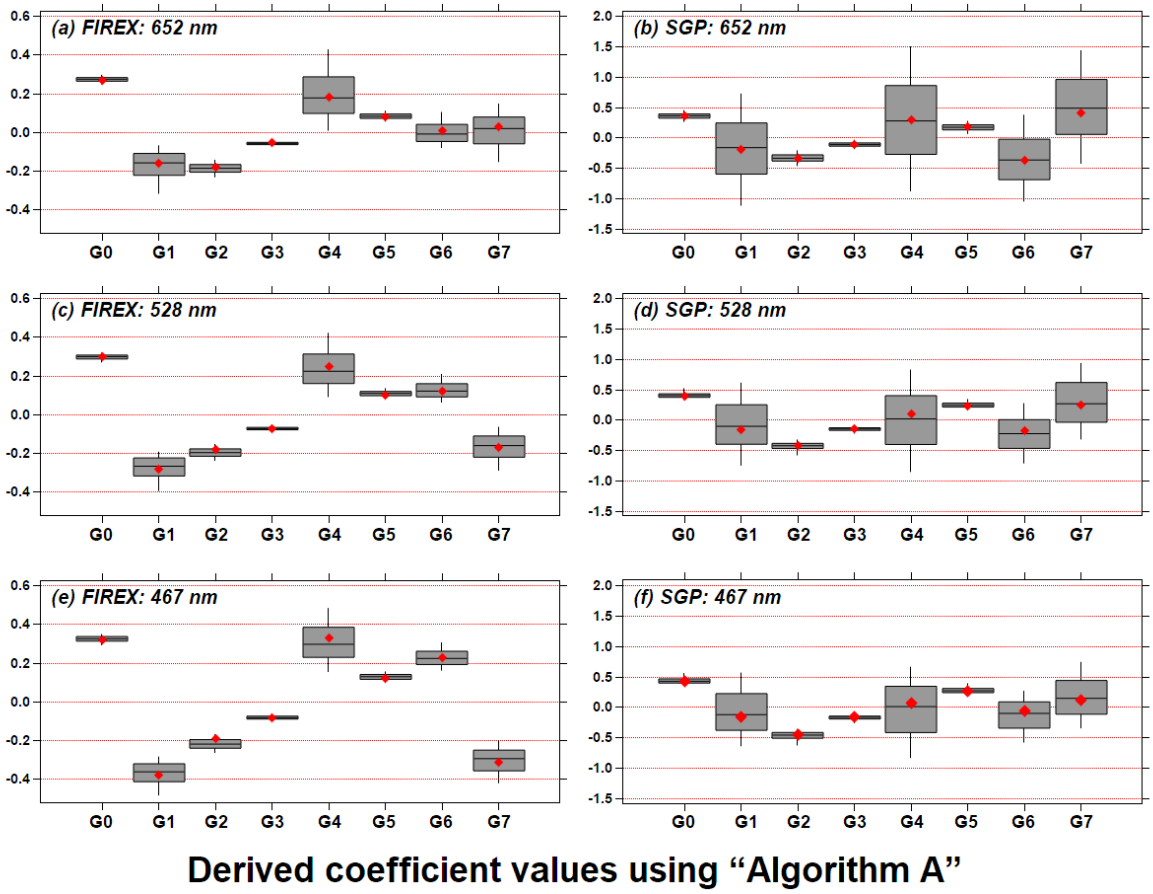

Figure S13. The distribution of derived coefficient values for Algorithm A using half of the CLAP observation. The red dots represent the coefficient values derived using all observations (as shown in Table 4).

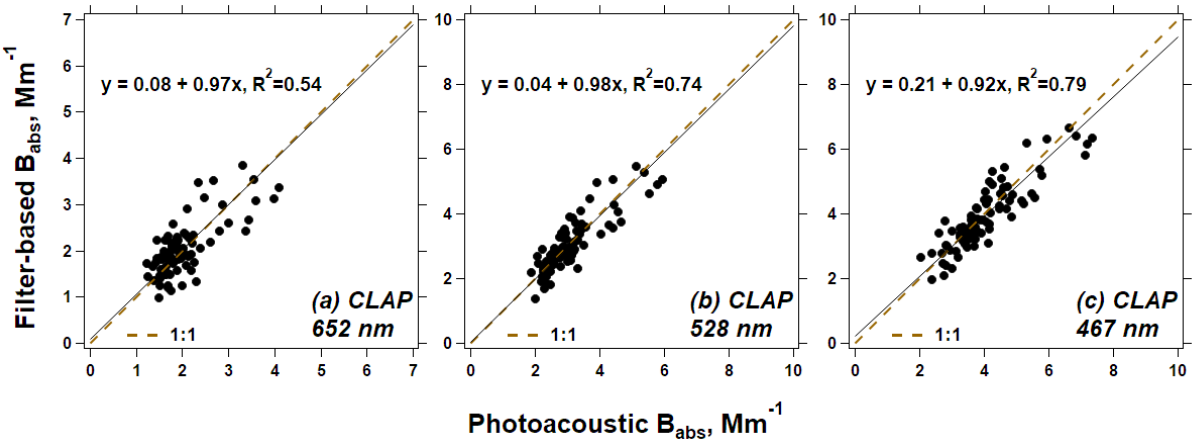

Figure S14. Inter-comparison between the CLAP-derived B_{abs} corrected by Algorithm C in the present work and reference B_{abs} at 652, 528, and 467 nm for the subsamples of SGP measurements (AAE-SSA prediction error is within 30%). The solid lines represent a linear regression, while the dashed lines are 1:1 lines.

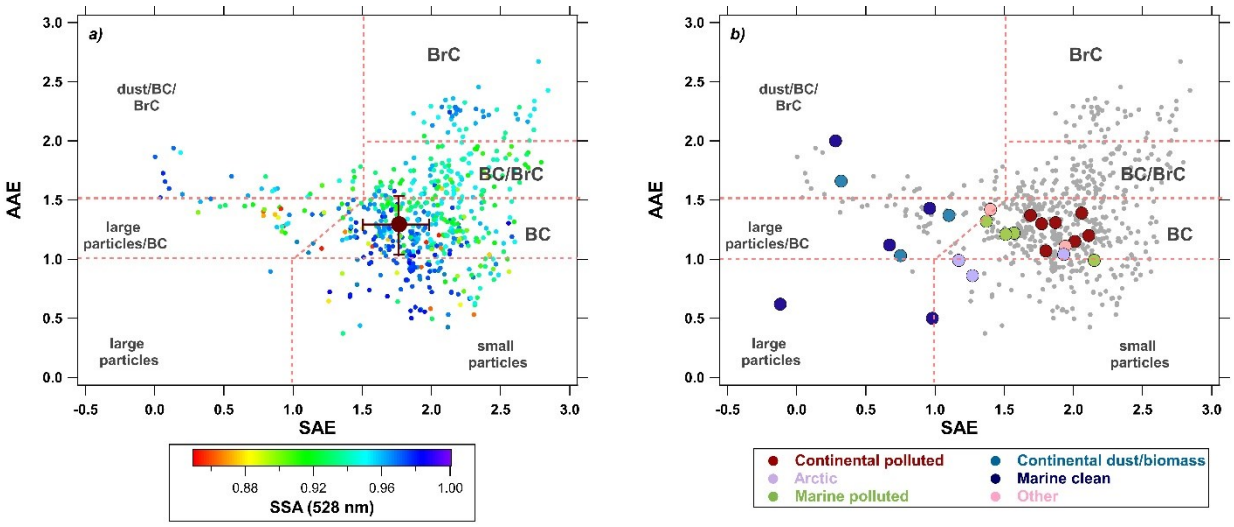

Figure S15. AAE vs. SAE for the SGP data. The three parameters are calculated using photoacoustic B_{abs} and Nephelometer B_{scat}. The panels are overlaid with the classification scheme presented in Cappa et al. (2016) and Schmeisser et al. (2017). In panel a), the averaged values (and standard deviation) of AAE and SAE reported for the SGP site in Schmeisser et al. (2017) are illustrated by the brown marker and error bars. Our results are colored by the corresponding SSA. In panel b), the results in Schmeisser et al. (2017) are colored by the corresponding type of station location and our results are colored in grey.

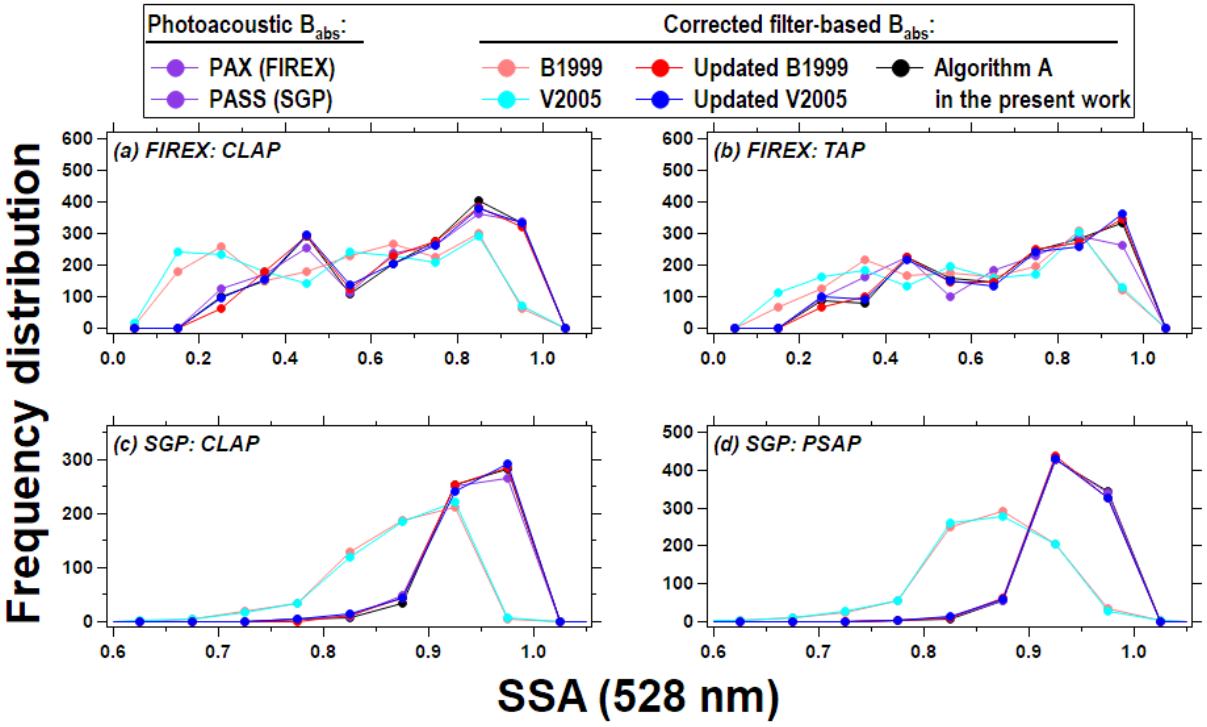

Figure S16. The frequency distribution of SSA (528 nm) calculated for different instrument/correction combinations of B_{abs} and B_{scat}.

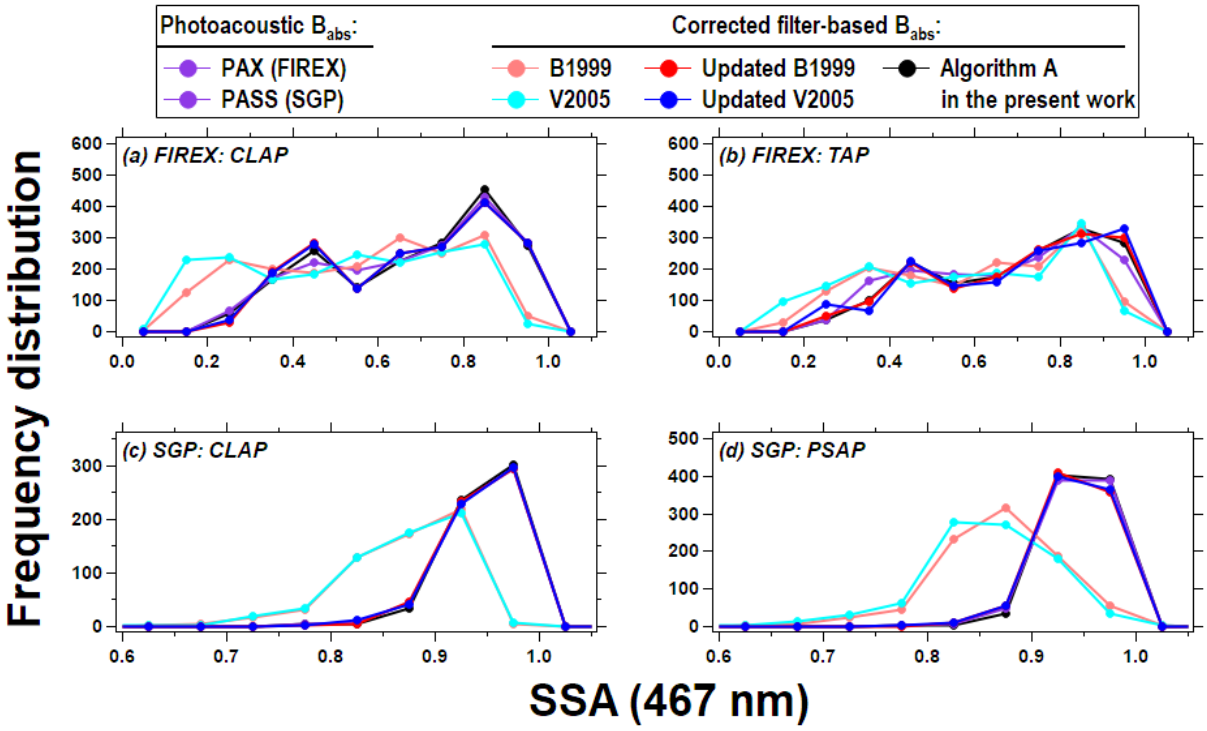

Figure S17. The frequency distribution of SSA (467 nm) calculated for different instrument/correction combinations of B_{abs} and B_{scat}.

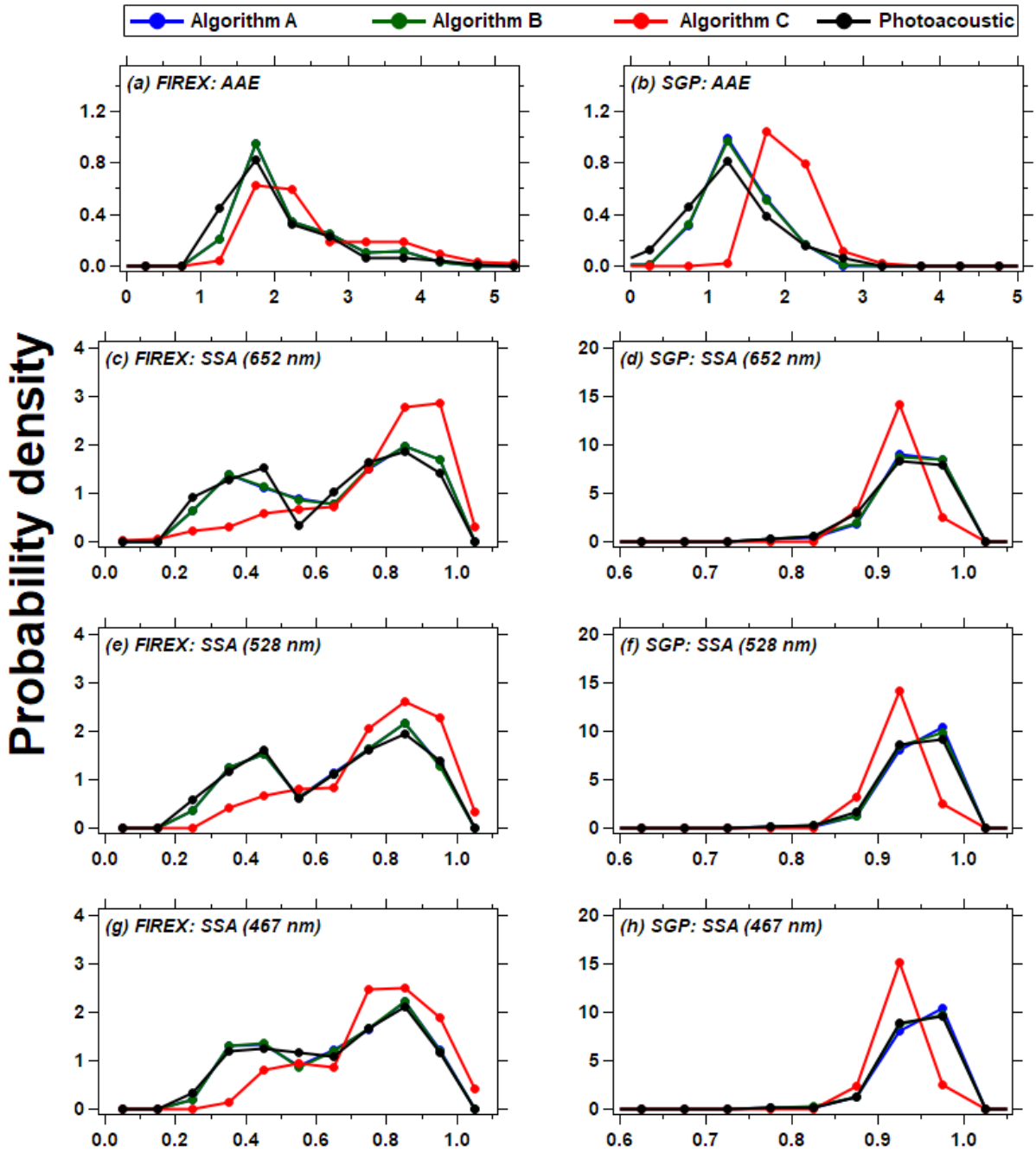

Figure S18. The probability density of AAE and SSA computed by the new algorithms (A, B, C) for the FIREX and SGP CLAP data. The curves of Algorithm A and Algorithm B overlap in some panels.

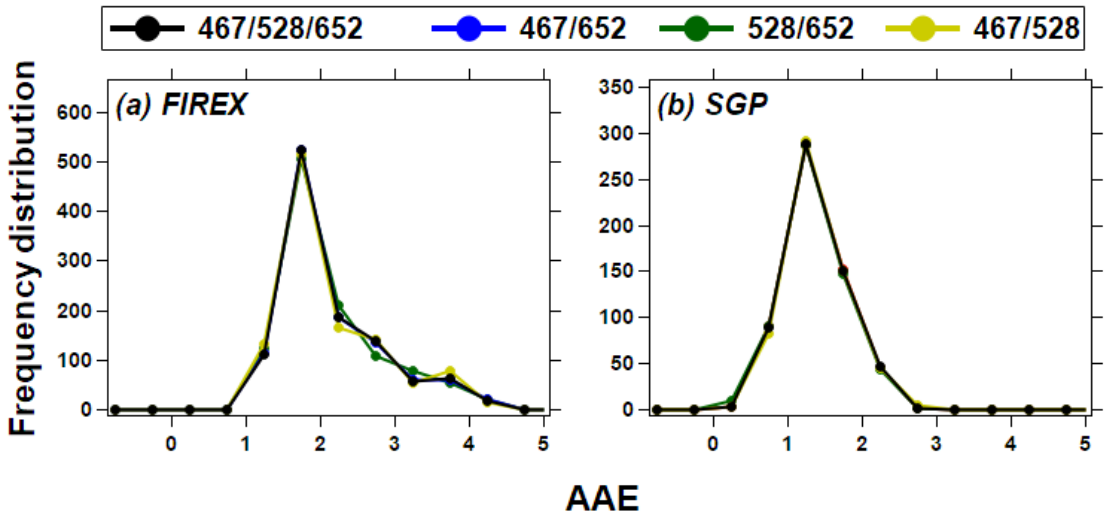

Figure S19. The frequency distribution of AAE calculated by different wavelength combinations (derived by Algorithm A in the present work).

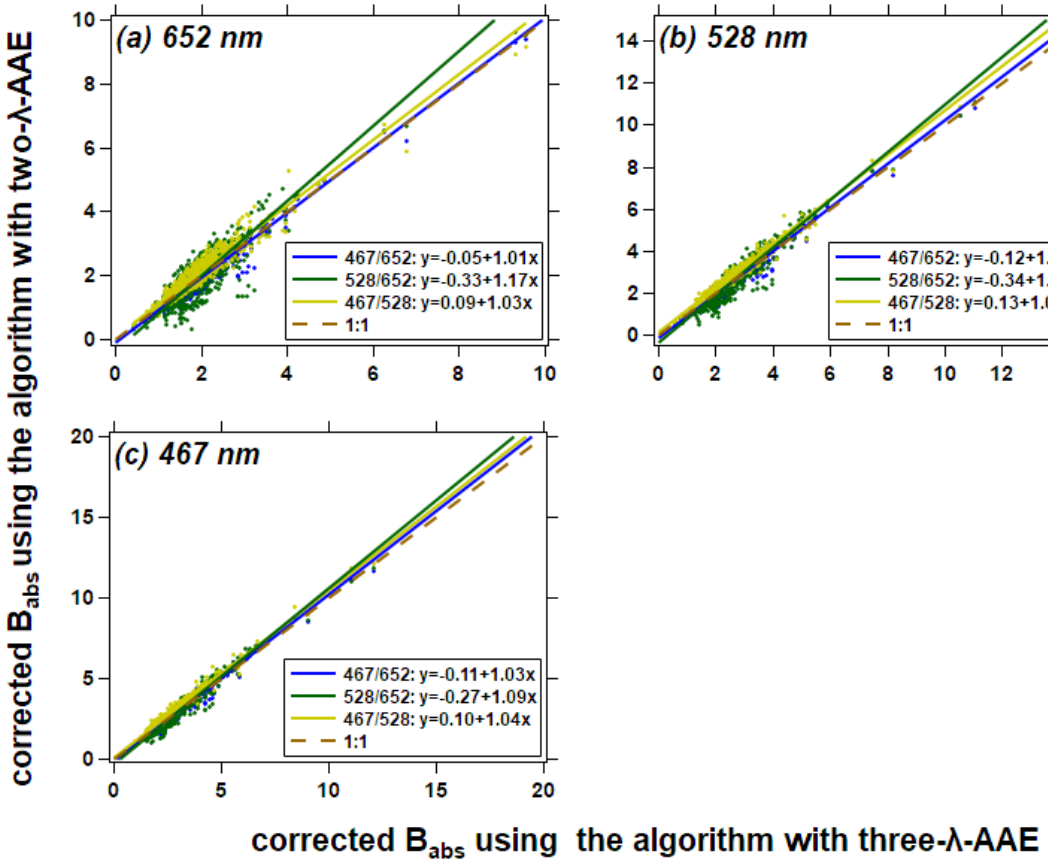

Figure S20. Inter-comparison of SGP-CLAP-B_{abs} derived by Algorithm A with different calculation of AAE.

REFERENCES

Aiken, L.S., West, S.G., Reno, R.R., 1991. Multiple regression: Testing and interpreting interactions. Sage.

Benoit, K., 2011. Linear regression models with logarithmic transformations. London Sch. Econ. London 22, 23–36.

Cappa, C.D., Kolesar, K.R., Zhang, X., Atkinson, D.B., Pekour, M.S., Zaveri, R.A., Zelenyuk, A., Zhang, Q., 2016. Understanding the optical properties of ambient sub- and supermicron particulate matter: results from the CARES 2010 field study in northern California. Atmos. Chem. Phys. 16, 6511–6535. https://doi.org/10.5194/acp-16-6511-2016

Creamer, D.B., Henyey, F., Schult, R., Wright, J., 1989. Improved linear representation of ocean surface waves. J. Fluid Mech. 205, 135–161.

Davies, N.W., Fox, C., Szpek, K., Cotterell, M.I., Taylor, J.W., Allan, J.D., Williams, P.I., Trembath, J., Haywood, J.M., Langridge, J.M., 2019. Evaluating biases in filter-based aerosol absorption measurements using photoacoustic spectroscopy. Atmos. Meas. Tech. 12, 3417–3434. https://doi.org/10.5194/amt-12-3417-2019

Dawson, J.F., Richter, A.W., 2006. Probing three-way interactions in moderated multiple regression: Development and application of a slope difference test. J. Appl. Psychol. 91, 917–926. https://doi.org/10.1037/0021-9010.91.4.917

Lek, S., Delacoste, M., Baran, P., Dimopoulos, I., Lauga, J., Aulagnier, S., 1996. Application of neural networks to modelling nonlinear relationships in ecology. Ecol. Modell. 90, 39–52.

Levenberg, K., 1944. A method for the solution of certain non-linear problems in least squares. Q. Appl. Math. 2, 164–168.

Müller, T., Virkkula, A., Ogren, J.A., 2014. Constrained two-stream algorithm for calculating aerosol light absorption coefficient from the Particle Soot Absorption Photometer. Atmos. Meas. Tech. 7, 4049–4070. https://doi.org/10.5194/amt-7-4049-2014

Nakayama, T., Kondo, Y., Moteki, N., Sahu, L.K., Kinase, T., Kita, K., Matsumi, Y., 2010. Size-dependent correction factors for absorption measurements using filter-based photometers: PSAP and COSMOS. J. Aerosol Sci. 41, 333–343. https://doi.org/10.1016/j.jaerosci.2010.01.004

Schmeisser, L., Andrews, E., Ogren, J.A., Sheridan, P., Jefferson, A., Sharma, S., Kim, J.E., Sherman, J.P., Sorribas, M., Kalapov, I., Arsov, T., Angelov, C., Mayol-Bracero, O.L., Labuschagne, C., Kim, S.-W., Hoffer, A., Lin, N.-H., Chia, H.-P., Bergin, M., Sun, J., Liu, P., Wu, H., 2017. Classifying aerosol type using in situ surface spectral aerosol optical properties. Atmos. Chem. Phys. 17, 12097–12120. https://doi.org/10.5194/acp-17-12097-2017

Zedeck, S., 1971. Problems with the use of "moderator" variables. Psychol. Bull. 76, 295–310. https://doi.org/10.1037/h0031543